

Multi-Layered Composite Electrodes of High Power $\text{Li}_4\text{Ti}_5\text{O}_{12}$ and High Capacity SnO_2 for Smart Lithium Ion Storage

Sang Ho Lee^{1,*}, Chun Huang² and Patrick S. Grant³

¹Department of Chemical Engineering, Pohang University of Science and Technology (POSTECH), Pohang 37673, South Korea.

²Department of Engineering, King's College London, London WC2R 2ND, UK.

³Department of Materials, University of Oxford, Oxford OX1 3PH, UK.

* Address correspondence to sangholee@postech.ac.kr

Abstract

Discrete layering of high power $\text{Li}_4\text{Ti}_5\text{O}_{12}$ and high capacity SnO_2 in a through-thickness multi-layered composite electrode was achieved using a layer-by-layer spray printing approach in order to explore new capacity-power combinations for lithium ion based electrochemical energy storage. Electrochemical behavior of multi-layered electrodes was optimized as a function of the thickness of the discrete SnO_2 layer, in the range 2 to 6 μm , interleaved between two layers of low volume expansion $\text{Li}_4\text{Ti}_5\text{O}_{12}$. Three discrete layers of 2 μm SnO_2 were then interleaved evenly between $\text{Li}_4\text{Ti}_5\text{O}_{12}$ layers to produce a “layer cake” negative electrode cross-section that offered remarkable rate capability when coupled with a spray printed LiFePO_4 positive electrode in a lithium ion battery arrangement. The multi-layered negative electrode was also coupled with a spray printed activated carbon positive electrode in a lithium ion capacitor configuration, providing significant improvements in energy density. The double-sided fabrication of the multi-layer electrode over a $20 \times 20 \text{ cm}^2$ current collector area suggested a possible hybrid electrochemical device that combines attributes of high capacity lithium ion batteries and high power lithium ion capacitors.

Keywords

Multi-layer composite, layer-by-layer spray printing, $\text{Li}_4\text{Ti}_5\text{O}_{12}$, SnO_2 , lithium ion battery, lithium ion capacitor.

1. Introduction

Electrochemical energy storage for mobile devices and hybrid/pure electric vehicles is currently dominated by lithium ion based rechargeable energy storage technologies. For example, lithium ion batteries (LIBs) have attractive gravimetric and volumetric energy density (~ 250 Wh/kg and ~ 650 Wh/L, respectively) but their power density (200-300 W/kg) is generally considered to be comparatively poor, principally due to the sluggish reaction kinetics of the enabling lithium ion intercalation mechanism.^[1-4] In practice, when significant power is required, simply more LIBs are added to the cell pack – due to their relatively low cost – but incurring weight and volume penalties, where arguably a more power dense storage technology would be preferable, such as lithium ion capacitors (LICs) that provide outstanding power capability (10-30 kW/kg) over thousands of charge/discharge cycles. Unfortunately, LICs suffer from a relatively low energy density (~ 20 Wh/kg) that undermines their otherwise advantageous attributes.^[5-8] In principle, a mixture of LIBs and LICs might offer the ability to “mix and match” energy and power characteristics in an optimized hybrid/integrated electrochemical energy storage system. However in practice, the engineering complexity, e.g. the power electronics required to balance LIC and LIB loads dynamically, may make such systems either too heavy, too bulky and/or unaffordable.

From a LIB negative electrode material point of view, high capacity materials such as Si, Sn, Ge and SnO₂ have been widely explored to boost energy density in lithium-based energy storage technologies.^[9-12] However, the strain of the associated large volume change in such materials on lithium ion insertion (up to 400 %) and the sluggish intercalation kinetics undermine performance at fast charging rates and reduce lifetime.^[13-15] To overcome such limitations and exploit

the intrinsic material capability more fully in full-cell performance, various approaches have been suggested, for example reducing the size of electrochemically active materials down to the nanoscale or designing nano-sized pores within electrode materials, both of which are intended to manage or relieve the induced strains more effectively.^[16-19] Recently, layering/coating approaches using so-called “buffering” materials have shown promise in reducing the particle volume expansion, or at least in reducing the most damaging effects of pulverization.^[20-22] However, the potential advantages of these approaches (that operate at the length-scale of the active material) may be obscured if the electrode manufacturing approach produces microstructural arrangements that do not allow these benefits to be realized. For example, conventional slurry casting routes typically require a relatively high fraction of polymeric binder for the mechanical stability of the resulting electrode.^[23,24] The use of binders tends to block interconnected porosity and active particle surfaces, and can be difficult to disperse homogeneously, especially during drying. When binder fractions increase locally, electrical resistance increases, and may produce a heterogeneous dispersion of over-potential across the electrode that can accelerate gravimetric/volumetric capacity degradation at high charge/discharge rates.^[25,26] Thus, to support particulate engineering approaches, compatible electrode manufacturing approaches should also be developed. In particular, more finesse in the structural and geometric local arrangement of electrochemically active and inactive components within electrodes may help to ensure that the intrinsic properties of active materials are realized more fully.^[27-32]

In this paper, we use a scalable spray printing approach to realize novel multi-layer composite electrodes comprising discrete layers of high power $\text{Li}_4\text{Ti}_5\text{O}_{12}$

(LTO) and high capacity SnO_2 that cannot be fabricated by conventional electrode manufacturing routes based on industry-standard slurry coating. Our hypothesis is that this approach can deliver a hybrid electrode with an unusual and more useful balance of capacity and power in a lithium ion based electrochemical energy storage device. Initially, a discrete layer of SnO_2 was located between two layers of LTO in a sandwich configuration, and half-cell performance was investigated as a function of SnO_2 thickness in the range 2 to 6 μm . Three discrete layers of the best performing 2 μm SnO_2 were then interleaved evenly between LTO-based multi-layers, giving remarkable improvements in energy and power performance in both LIB and LIC configurations when paired with spray printed LiFePO_4 (LFP) and activated carbon (AC) positive electrodes, respectively. The multi-layered hetero-electrode was then fabricated over $20 \times 20 \text{ cm}^2$ electrode areas in a double-sided configuration, and a hybrid concept that combined LIC and LIB configurations in a single device format was suggested. This type of hybridization design approach – enabled by a new manufacturing approach – may provide new ways of developing lithium ion energy storage technologies with targeted capacity-power combinations.

2. Results and discussion

Figure 1 shows schematically the multi-layer fabrication of discrete layers of high power LTO and high capacity SnO₂, layer-by-layer, into a single electrode configuration by spray printing. The aim was to develop an efficient electrode design that would tolerate the induced electrode strains due to the large volume expansion/contraction of the high capacity SnO₂ without excessive cycle fading on charge/discharge, while the intrinsic high power capability of the majority LTO was retained. The resulting hybrid- or hetero-electrode was investigated in both LIB and LIC configurations.

To produce a stable suspension suitable for large area spray printing, the electrochemically active materials (LTO or SnO₂), carbon conductive enhancers (Super P, SP) and polymeric binders (carboxymethyl cellulose, CMC) were dissolved/suspended in a fugitive bi-solvent mixture of 70 vol% deionized water (DI) and 30 vol% isopropyl alcohol (IPA). Addition of IPA was required to ensure an adequate dispersion of the SP carbon in the predominantly aqueous suspension. The resulting relatively dilute ($\sim 5 \times 10^{-3}$ g/mL) and low viscosity feedstock suspension was pumped peristaltically into an atomizing spray nozzle operated with compressed air. The resulting cone-shaped spray of suspension droplets was then projected onto a heated foil current collector. On deposition, the suspension droplets dried almost immediately, and the successive superimposition of more and more droplets built up progressively the electrode directly on the current collector foil, as the spray cone scanned over the surface in a repeating zig-zag pattern. Suspension and spray parameters were chosen to promote rapid drying and to avoid any re-suspension of the solid components at the interface between subsequent sprayed layers. This layer-by-layer approach to build up the electrode enables a wide design

freedom for multi-layer arrangements simply by switching between feedstock suspension types at will, as shown in Figure 1. Each deposited layer can be as thin as a few microns (depending on the suspended particle size), and up to $\geq 100\ \mu\text{m}$ or more simply by controlling the number of deposition cycles and/or the solid concentration of the feedstock suspensions. “On the fly” mixing of suspensions to create graded electrodes is also readily achievable.^[25,26]

Based on recent work on high capacity but usually low cycle life intercalation hosts such as Si dispersed as discrete layers in LIB negative electrodes,^[33] it was hypothesized that a relatively thin (a few microns) discrete SnO_2 layer interleaved between two layers of high power LTO may withstand the pulverizing strains of intercalation more effectively than a SnO_2 -only electrode. This is suggested to arise because the low expansion outer layers mechanically buffer the expansion of the high expansion inner layer, so that harmful expansion strains are not propagated throughout the entire electrode. Therefore, a LTO layer was deposited first on the current collector, followed by a comparatively thin SnO_2 layer on the LTO, and finally a LTO- SnO_2 -LTO sandwich configuration was completed by depositing a 2nd layer of LTO on the SnO_2 , as shown schematically in Figure 2a. The electrochemical behavior of the multi-layer arrangement was then investigated as a function of the SnO_2 -based layer thickness to identify an optimum arrangement whereby the unhelpful intercalation strain of SnO_2 did not deteriorate overall electrode performance.

Figures 2b-e exhibit a series of scanning electron microscope (SEM) images of multi-layer electrode cross-sections prepared using the precision etching and coating system (PECS) milling. As the SnO_2 thickness increased progressively from 0 to $6\ \mu\text{m}$, the LTO thickness decreased from 20 to $14\ \mu\text{m}$ correspondingly, so that

the overall electrode thickness was maintained at $\sim 20\ \mu\text{m}$ for all cases. In each case, the right-upper inset images magnify the region of the SnO_2 within the multi-layers. The left-hand inset cartoons depict the progressive change in the SnO_2 layer thickness. We chose a relatively thin $20\ \mu\text{m}$ electrode because our focus was principally on high power and high capacity and much thicker electrodes tend to undermine high power performance. However, it would be trivial to reverse the LTO and SnO_2 proportions and locations, and a thicker electrode can be easily produced if the focus was to prioritize capacity over power.

Figure S1 in the Supporting Information shows representative energy-dispersive X-ray spectroscopy (EDS) elemental map images for Ti (yellow) and Sn (blue) from a multi-layered electrode with a $2\ \mu\text{m}$ SnO_2 inter-layer, showing the discrete LTO and SnO_2 layers and very limited inter-layer mixing. SEM images and X-ray diffraction (XRD) patterns for pristine particles of LTO and SnO_2 are given in Figure S2 of the Supporting Information, indicating particle diameters of $\sim 80\ \text{nm}$ and $\sim 50\ \text{nm}$, respectively, and confirming the expected crystalline phases.^[34-37]

Figure 3a shows half-cell cyclic voltammetry (CV) profiles at a constant scan rate of $0.1\ \text{mV/s}$ for the 1st cycle for LTO-only, SnO_2 -only and multi-layered electrodes. For the LTO-only electrode (yellow), there were two pairs of anodic/cathodic peaks at approximately $0.3\ \text{V}/0.4\ \text{V}$ and $1.7\ \text{V}/1.3\ \text{V}$, which were typical of spinel LTO in the potential range 0.05 to $2.5\ \text{V}$ (vs. Li/Li^+).^[38,39] However, for a multi-layer (blue) electrode there were additional strong peaks at approximately $0.5\ \text{V}/0.7\ \text{V}$ that were associated with the intercalation reaction of lithium ions in SnO_2 , and consistent with the CV curve of SnO_2 -only (grey).^[40,41] The left-hand inset shows the gravimetric charge/discharge profiles at $20\ \text{mA/g}$ for the 1st cycle of the LTO-only, SnO_2 -only and multi-layer electrodes, while the right-

hand inset magnifies the discharge curves for the LTO-only and multi-layer electrodes in the potential range 0.0 to 1.75 V. For the SnO₂-only and multi-layer electrodes, there was a voltage plateau at approximately 0.7 V that was associated with the well-known solid electrolyte interface (SEI) formation on SnO₂, causing an irreversible capacity loss in the first cycle.^[40-42]

Figure 3b shows the gravimetric discharge capacity profiles for the same electrodes as a function of charge/discharge current densities in the range 20 to 4000 mA/g. For current densities of 20 to 400 mA/g, electrode capacities increased proportionally as the SnO₂ thickness increased from 2 to 6 μ m, as given in Table 1. However, as the current density continued to increase to 4000 mA/g, the proportional effect of a thicker SnO₂ layer reduced gradually. For example, at 800 mA/g the multi-layer electrodes had similar capacities regardless of the SnO₂ layer thickness, while at 4000 mA/g, the multi-layered electrode with 2 μ m SnO₂ had the highest discharge capacity of \sim 200 mAh/g while the 6 μ m SnO₂ had a capacity reduced to \sim 180 mAh/g, both of which were nonetheless superior to LTO-only (\sim 160 mAh/g). Further details are given in Table 1. This tendency was predominantly due to the problematic volume expansion and more severe pulverization of thicker SnO₂ layers,^[40-42] and a comparatively thick SnO₂ layer was most advantageous in terms of capacity only at the lowest current densities. The inset bar in Figure 3b summarizes the capacity degradation trend with increasing rate as a function of SnO₂ thickness. As shown in Figure S3 of the Supporting Information, if an even thinner layer was introduced (\sim 1 μ m), overall capacity increased slightly over LTO-only, but was less effective than a 2 μ m layer at all current densities studied.

Any intrinsic beneficial effect of multi-layering was studied by comparing layered electrodes with similar electrodes comprising randomly mixed LTO and

SnO₂, also prepared through spray printing, and comprising the same weight fractions of LTO and SnO₂ as the 6 μ m SnO₂ multi-layer electrode, i.e. a random mix electrode with active materials comprising 80 wt% LTO and 20 wt% SnO₂. Figure 3b shows that at 20 mA/g and 40 mA/g, the random-mix electrode delivered capacities comparable with the multi-layer equivalent, but capacity faded more rapidly as current density increased to 4000 mA/g. Eventually, the capacity of the random-mix electrode was even lower than that of the LTO-only electrode at 4000 mA/g (Table 1), implying that SnO₂ delivered extra performance benefits only at high current density when present as a discrete layer. These data support the hypothesis that encapsulating a layer of high capacity, high volume expansion SnO₂ between two layers of low volume expansion LTO may provide some mechanical buffering of the strains induced in the SnO₂ on charge/discharge.

Figure 3c shows galvanostatic discharge capacity profiles at a constant charge/discharge current density of 400 mA/g. In the initial charge/discharge cycles, the multi-layer and random-mix electrodes had similar deliverable discharge capacities. However, after 50 cycles the difference in deliverable electrode capacities became more marked as a function of electrode configuration, depending on how effectively the problematic pulverizing volume expansion in the SnO₂ was accommodated within the multi-layer arrangement. Eventually, after 300 cycles the multi-layer electrode with 2 μ m SnO₂ sustained a capacity of \sim 250 mAh/g that was superior to the 6 μ m SnO₂ case (\sim 190 mAh/g). The random-mix electrode delivered a capacity of only \sim 80 mAh/g that was again lower than the LTO-only (\sim 160 mAh/g). The inset shows the corresponding fractional capacity retention. Multi-layers with 2, 4 and 6 μ m SnO₂ had comparatively poor capacity retentions of 60 %, 55 % and 50 % after 300 cycles, respectively, all of which were lower than the

LTO-only ($\sim 65\%$) electrode, which is known to be relatively tolerant to cycling due to its near zero insertion strain.^[43-45] The inferior capacity retention of SnO_2 containing electrodes was likely associated with unhelpful pulverization and repeated SEI formation on SnO_2 over cycles.

To utilize the performance benefit of SnO_2 more fully in the multi-layer electrode, the effect of interleaving three discrete layers of the best performing $2\ \mu\text{m}$ SnO_2 , into the LTO electrode, was investigated. This would allow for an assessment of whether a number of discrete thin SnO_2 layers were superior or inferior to a relatively thick single SnO_2 inter-layer.

Figure 4a shows a representative electrode cross-section SEM image of the three discrete layers of $2\ \mu\text{m}$ SnO_2 within a $20\ \mu\text{m}$ thick LTO-based electrode formed layer-by-layer, and denoted as “LbL”. The comparable single SnO_2 layer arrangement is shown in Figure 4b. The left-upper inset cartoons depict the multi-layers, and the EDS map images in the right-hand insets identify Sn in the multi-layers.

Figure 4c shows the corresponding half-cell performance of the same multi-layer electrodes. Here, the charge/discharge current density alternated between $20\ \text{mA/g}$ and $4000\ \text{mA/g}$ after each of 5 charge/discharge cycles, aiming to assess both high rate capability and cycle stability simultaneously. As charge/discharge cycles progressed repeatedly to the 105th cycle, the LbL electrode retained higher discharge capacities than the multi-layer electrode containing a single $6\ \mu\text{m}$ SnO_2 layer. For instance, after 105 cycles at $20\ \text{mA/g}$ (the blue region) the LbL electrode delivered a recovered discharge capacity of $\sim 325\ \text{mAh/g}$ while the capacity of the $6\ \mu\text{m}$ SnO_2 electrode reduced to $\sim 265\ \text{mAh/g}$, corresponding to $\sim 85\%$ and $\sim 70\%$ capacity retention of the 2nd cycle discharge capacity ($\sim 380\ \text{mAh/g}$ for both

electrodes), respectively, as shown in Figure 4d. At the 100th cycle cycled at a high current density of 4000 mA/g (the yellow region), the LbL electrode had a superior discharge capacity of ~ 165 mAh/g over the multi-layer with 6 μ m SnO₂ (~ 70 mAh/g), showing ~ 44 % and ~ 18 % of capacity retention based on the 2nd cycle discharge capacity, respectively, as shown in Figure 4e. In both electrodes however, SnO₂ pulverization gradually undermined capacity retention. Factoring in the relatively poor retention of the random mix electrode also, it can be concluded that while some fading of electrodes containing SnO₂ was unavoidable, capacity retention was optimized when the SnO₂ was present in thin, discrete layers.

Figure S4 in the Supporting Information shows typical cross-section SEM images of the LbL electrode after 105 charge/discharge cycles. Although the layer thickness increased as expected due to the volume expansion of SnO₂, the layer remained continuous and discrete, and the overall multi-layer architecture was well-preserved.

The half-cell performance of spray printed LTO-only, SnO₂-only and LbL electrodes is compared in Figure S5 of the Supporting Information (also see Table S1). At 20 mA/g, the SnO₂-only electrode had a discharge capacity of ~ 800 mAh/g that was much higher than both the LTO-only and LbL electrodes (~ 240 mAh/g and ~ 380 mAh/g, respectively). However, the capacity reduced drastically to only ~ 20 mAh/g as current densities increased to 4000 mA/g. By contrast, the LbL electrode delivered a capacity of ~ 210 mAh/g at 4000 mA/g.

Comparing half-cell performance with data from the literature in Table S2 of the Supporting Information shows that the LbL electrode had better rate capability than other composite electrodes comprising LTO-based active components randomly mixed with a small fraction of high capacity additives (e.g. Si, Sn or

SnO₂). Table S2 shows that performance benefits of high capacity additives at relatively low rates were undermined comparatively quickly as current density (or C-rate) increased.

To understand why the LbL configuration delivered superior rate performance at high charge/discharge current densities over other composite-type electrodes, we investigated the lithium ion mobility behavior on the basis of the electrochemical response of the SnO₂. Figures 5a-c exhibit a series of CV profiles at increasing scan rates from 0.05 to 1.00 mV/s for half-cells of the LbL, 6 μ m SnO₂ multi-layer and random-mix electrodes, respectively, i.e. all the electrodes contained the same fraction of SnO₂ but with differing micro-arrangements of the SnO₂. As the scan rate increased, anodic/cathodic peak current density at approximately 0.7 V/1.1 V associated with lithium intercalation in SnO₂ increased markedly for the LbL electrode, but much less for the 6 μ m SnO₂ and random-mix electrodes, again suggestive of the advantageous attributes of thinner, discrete SnO₂ layers.

Figure 5d shows the best-fit linear fit of the anodic peak current density at approximately 0.7 V to the square root of the scan rate for the same electrodes. Given the good fit, it is possible to estimate the effective lithium ion mobility for the SnO₂ part of the electrode using the Randles-Sevcik equation.^[46,47]

$$I_p = 0.4463n F A C_0 (n F v M_{Li} / RT)^{1/2} \quad (1)$$

where I_p was the peak current [A], n was the number of electrons transferred during the reaction, F was the Faraday constant [C/mol], A was the effective electrode area used [cm²], C_0 was the molar density in the electrode [mol/cm³], v was the CV scan

rate [V/s], M_{Li} was the effective lithium ion mobility [cm^2/s], R was the gas constant [$\text{J/K}\cdot\text{mol}$] and T was temperature [K].

Equation (1) is generally used for a homogenous dispersion of electrode components, whereas two of the electrodes studied here had deliberate hetero-structures, and thus interpretation requires caution. Nonetheless, since diffusion controlled energy storage reactions in SnO_2 were involved (Figure 5d), some insight into the local lithium ion mobility within the SnO_2 -rich region was useful.

Figure 5e shows the LbL electrode had the highest lithium ion mobility in SnO_2 -rich regions of $\sim 8 \times 10^{-13} \text{ cm}^2/\text{s}$, higher than the $6 \mu\text{m}$ SnO_2 electrode ($M_{\text{Li}} \sim 5 \times 10^{-13} \text{ cm}^2/\text{s}$), and almost three times that of the random-mix electrode ($M_{\text{Li}} \sim 3 \times 10^{-13} \text{ cm}^2/\text{s}$). Because the overall mass loading and composition of the three electrode types were otherwise identical, it was assumed that micro-variations in the SnO_2 arrangement were the critical factor controlling changes in the effective lithium ion mobility.

The sensitivity of ion mobility estimates to SnO_2 position was rationalized as follows. First, although it was difficult to accurately quantify the local porosity fraction in the $2 \mu\text{m}$ and $6 \mu\text{m}$ thick SnO_2 -only layers, Figure S4 in the Supporting Information suggested that SnO_2 layers typically had a higher local pore fraction than LTO layers. Thus, lithium ion mobility was enhanced in discrete SnO_2 -only layers compared with SnO_2 dispersed throughout the electrode. Second, as charge/discharge current densities (or scan rates) increased, a through-thickness gradient in the local ion concentration tends to develop: a higher local concentration of active ions in regions close to the separator and the counter electrode than in regions adjacent to the current collector. Under ion gradient conditions, SnO_2 is more sensitive than LTO to its precise through-thickness location because of its

much larger capacity for ions. Thus, discrete SnO₂ layers in the LbL configuration ensured that most of the SnO₂ was located in regions of comparatively high active ion concentration, whereas a random arrangement ensured a fraction of SnO₂ was dispersed into regions of relatively low active ion concentration (e.g. close to the current collector), and could not contribute fully to the electrode electrochemical response.

We further explored capacitive- and diffusion-controlled contributions to better understand electrode dynamics at increasing charge/discharge rates in the CV plots in Figures 5a-c using Equation (2).^[48-50]

$$I(V) = k_1v + k_2v^{1/2} \quad (2)$$

where $I(V)$ was the current density at a certain voltage [mA], k_1 and k_2 were best-fit constants and v was the CV scan rate [mV/s]. The first term on the right-hand side of Equation (2) represents the current density due to pseudocapacitive charge storage (k_1v) while the second term represents the diffusion-controlled capacity associated with insertion reactions ($k_2v^{1/2}$). Equation (2) is usually applied for very high specific area materials – typically nanomaterials – where fast surface reactions (sometimes termed “pseudocapacitance” faradic reactions) can make a significant contribution to capacity.^[51,52] The LTO and SnO₂ had mean diameters of 80 nm and 50 nm respectively, and suggested the use of Equation (2) may be applicable. Figures 6a-c show the estimated capacitive-controlled electrode responses (the patterned areas) at a scan rate of 0.1 mV/s for each of the LbL, 6 μ m SnO₂ multi-layer and random-mix electrodes. The comparative bar graphs in Figure 6d show corresponding estimates of the capacitive to diffusive contributions for the same

electrodes as a function of CV scan rate. At 0.05 mV/s, the three electrodes had almost the same capacitive contribution of ~ 30 %. As the scan rate increased to 1 mV/s, the capacitive contribution ratio increased progressively (i.e. the diffusion contribution decreased correspondingly), and the difference in the capacitive contribution between the electrodes became more marked, as summarized in Figure 6e. For instance, at 1 mV/s the LbL configuration showed the highest capacitive contribution of ~ 70 %, while the random-mix electrode had a capacitive contribution of ~ 50 %. The higher percentage of the surface-induced pseudocapacitive effect ensured higher deliverable capacities at increasing rates. Thus, the LbL arrangement was beneficial in terms of electrode reaction kinetics as well as buffering the more severe effect of intercalation strains in SnO₂.

The LbL electrode was also investigated in a LIB configuration coupled with a spray printed LFP positive electrode (the LFP electrode half-cell performances are given in Figure S6 and Table S3 in the Supporting Information). The LbL-based LIB performance was compared with a similar LIB using a LTO-only negative electrode and the same LFP-based positive electrode. Figure 7a shows the LIB gravimetric capacity degradation at increasing current densities of 20 to 4000 mA/g. The LbL electrode delivered higher discharge capacities than the LTO-only equivalent at all rates, as also given in Table 2, noting that the LIB capacity was estimated based on the total mass of active materials in the negative electrodes (e.g. the mass of LTO plus SnO₂). Figure 7b shows the corresponding volumetric capacity charge/discharge curves, where the volumetric capacities were calculated by normalizing the gravimetric capacities by the mass and thickness of the negative electrodes, as given in Table 2. Consistent with the gravimetric performance, the LbL LIB was again superior, for example with volumetric discharge capacities of

$\sim 320 \text{ mAh/cm}^3$ at 20 mA/g and $\sim 165 \text{ mAh/cm}^3$ at 4000 mA/g . Figure 7c shows the galvanostatic discharge capacity profiles at a constant charge/discharge current density of 400 mA/g for the LIBs using the LbL and LTO-only negative electrodes, with discharge capacities of $\sim 125 \text{ mAh/g}$ and $\sim 80 \text{ mAh/g}$ after 500 cycles, respectively. The LIBs had almost 100 % coulombic efficiency after 500 cycles (the right-hand inset), excluding the first few cycles of the LbL-based LIB associated with the irreversible SEI formation. The left-hand schematic shows the best performing LIB arrangement with a LbL negative electrode.

We also investigated any performance benefit of the LbL hetero-electrode in a LIC configuration, and if high capacity SnO_2 could boost overall capacity in an arrangement more specifically configured for power performance. Figure 8a shows comparative Ragone plots of LICs using the LbL electrodes paired with spray printed AC-based positive electrodes. The electrochemical behavior of the AC-based half-cells is given in Figure S7 and Table S4 in the Supporting Information. The LIC using a LTO-only electrode delivered 55 Wh/kg at 9 W/kg and 8 kW/kg at 15 Wh/kg , whereas the LIC using the LbL hetero-electrode delivered 90 Wh/kg at 15 W/kg and 15 kW/kg at 30 Wh/kg . Note, LIC performance was estimated using the mass of all active materials in both negative and positive electrodes (e.g. LTO, SnO_2 and AC).

Figure 8b shows the charge/discharge curves for the same LICs using the LbL and LTO-only electrodes. Capacitance was estimated using $C [\text{F/g}] = i \times t / V$, where i was the applied current $[\text{A/g}]$, t was the discharging or charging time $[\text{s}]$, and V was the potential difference $[\text{V}]$.^[53,54] At relatively high current densities of 2.5 A/g and 4.2 A/g , the LbL hetero-electrode provided deliverable capacitances of $\sim 50 \text{ F/g}$ and $\sim 35 \text{ F/g}$, respectively, almost double those of the LTO-only electrode (\sim

27 F/g at 2.5 A/g and ~ 17 F/g at 4.2 A/g), as indicated in Table 3. Figure 8c shows galvanostatic discharge energy density profiles at 1000 mA/g for the same LICs, with the corresponding charge/discharge energy density curves given in Figure S8 of the Supporting Information. After 2000 cycles, the LbL and LTO-only electrodes sustained energy densities of ~ 56 Wh/kg and ~ 32 Wh/kg, respectively, representing $\sim 75\%$ and $\sim 80\%$ of the initial energy density (~ 75 Wh/kg and ~ 40 Wh/kg in the 1st cycle), respectively. The relatively fast degradation in energy density of the LbL electrode in the first few cycles was attributed to irreversible capacity loss by the SEI formation on SnO₂, as previously identified in the LIB configuration. The left-hand schematic represents the current flow within the LbL-based LIC configuration during charge/discharge processes.

Overall, the LbL hetero-structure approach provided a new perspective on how to use effectively potentially attractive high capacity materials that usually suffer from well-known problems of pulverization and severe capacity fade. Some of the benefits of the LbL approach for LIBs and LICs are summarized in the Ragone plot shown in Figure 9a where the total mass of active materials in both negative and positive electrodes was used for gravimetric normalization. While the LbL-based LIB delivered a higher energy density (~ 300 Wh/kg) than the LbL-based LIC (~ 90 Wh/kg), the LIC had a power capability (~ 15 kW/kg) that was an order of magnitude greater than the LIB (~ 1 kW/kg). The inset image also shows that the LbL electrode was successfully fabricated over a $\sim 20 \times 20$ cm² current collector area that could involve selectively patterned regions through a use of a simple masking arrangement. A double-sided fabrication approach could be used to enable a hybridized high capacity LIB and high power LIC configuration within a single device arrangement, as shown schematically in Figure 9b. A converter inter-

connected between the LIC and the LIB would facilitate and manage discharge and recharge cycles under either high power or longer term high capacity conditions.

3. Conclusions

Through-thickness multi-layered electrode hetero-architectures were fabricated over large area current collectors ($\sim 20 \times 20 \text{ cm}^2$) using spray printing of high power LTO and high energy SnO_2 . The thickness and therefore weight fraction of SnO_2 in the LTO-based $20 \text{ }\mu\text{m}$ thick composite electrode in a sandwich configuration was studied in detail. A relatively thick $6 \text{ }\mu\text{m}$ SnO_2 layer was effective in boosting energy density only at relatively low current densities, while a relatively thin $2 \text{ }\mu\text{m}$ SnO_2 layer retained useful capacities even at high current densities. Then, three discrete layers of $2 \text{ }\mu\text{m}$ SnO_2 were interleaved evenly in a LTO-based hetero-electrode, layer-by-layer. The resulting LbL electrode delivered an attractive energy density in a LIC configuration and a marked power capability in a LIB arrangement when paired with spray printed counter electrodes. We anticipate that an integrated LIB/LIC device contrived by a double-sided LbL electrode might be a promising approach to negotiate the inevitable trade-offs between overall cell capacity and power in lithium ion based electrochemical energy storage technologies. The spray printing approach provided new flexibility to develop bespoke electrode designs that was unavailable by conventional electrode manufacturing routes (e.g. slurry casting), including exploiting complementary material combinations, controlling electrode thicknesses, and/or managing the spatial arrangement of active and non-active materials within the electrodes.

4. Material and methods

Materials: LTO, SnO₂ and CMC were obtained from Sigma Aldrich, UK; SP from MTI Corporation, USA; AC (YP-50F) from Kuraray, Japan; and LFP from Hydro-Québec, Canada.

Spray printed electrodes: For the spray suspension, active materials (LTO, SnO₂, LFP or AC), SP and CMC in a controlled mass ratio of 80:10:10 were blended into a 70:30 bi-solvent mixture (by volume) of DI and IPA by ultra-sonication. For the suspension used to fabricate electrodes with randomly-mixed materials throughout, LTO, SnO₂, SP and CMC in the mass ratio of 64:16:10:10 were dissolved and mixed into the same volume fraction of DI and IPA. A Cu foil current collector was fixed on a vacuum chuck that was then heated to a temperature high enough to evaporate both the IPA and DI water, typically > 100 °C. The suspension was then pumped to a spray nozzle and subsequently atomized into droplets by compressed air in the range 30 to 50 kPa. The atomizing nozzle moved over the heated current collector according to a pre-set computer program, e.g. a zig-zag pattern in *x* and *y* plane and a constant spray distance *z*. To form in-plane electrode patterns, a shadow mask was placed on the current collector or pre-deposited layers. The next layer was then spray deposited through the mask. Before SEM investigations, electrode cross-sections were prepared using a Gatan PECS II system. SEM and EDS images were obtained in a Zeiss Merlin Analytical SEM without metal pre-coating.

Electrochemical testing: The electrochemical performance of spray printed electrodes was examined using coin-type electrochemical cells (CR2032) that were assembled in an Ar-filled glovebox (H₂O < 0.1 ppm, O₂ < 0.1 ppm). For half-cells, working electrodes were coupled with high purity lithium chips (99.9% trace metals basis, MTI Corporation, USA) that were used as a counter/reference electrode. For

the full-cell assembly, LIBs were formulated with an anode:cathode capacity ratio of 1:1, given in Table 2, while LICs were formulated with an anode:cathode mass ratio of 1:4, given in Table 3. LIC cells were manufactured without a pre-lithiation process. Positive and negative electrodes were electrically separated by a polypropylene separator (Celgard 2400, UK) soaked into 1 M LiPF_6 electrolyte solution in a mixture of 50 vol% ethylene carbonate and 50 vol% dimethyl carbonate (Sigma-Aldrich, UK). Charge/discharge cycles and CV tests were conducted at room temperature using Arbin BT2000 cyclers and Gamry 600 potentiostats, respectively. The theoretical capacity of LTO, SnO_2 and LFP was assumed to be $\sim 175 \text{ mAh/g}$,^[43] $\sim 780 \text{ mAh/g}$ ^[12] and $\sim 170 \text{ mAh/g}$,^[55] respectively.

Acknowledgments

This work was supported by the UK Engineering and Physical Science Research Council through Grant EP/M009521/1 “Enabling Next Generation Li-ion Batteries”, the Faraday Institution grant number FIRG015 and a UK UKRI Innovation Fellowship EP/S001239/1. The authors would like to thank Hydro-Québec for providing the LFP materials.

References

- [1] C. M. MacLaughlin, *ACS Energy Lett.* 4 (2019) 786-788.
- [2] M. Li, J. Lu, Z. Chen, *Adv. Mater.* 30 (2018) 1800561.
- [3] A. I. Inamdar, R. S. Kalubarme, J. Kim, Y. Jo, H. Woo, S. Cho, S. M. Pawar, C. -J. Park, Y. -W. Lee, J. I. Sohn, S. Cha, J. Kwak, H. Kim, H. Im, *J. Mater. Chem. A* 4 (2016) 4691-4699.
- [4] S. Liu, J. Feng, X. Bian, Y. Qian, J. Liu, H. Xu, *Nano Energy* 13 (2015) 651-657.
- [5] Y. Hao, S. Wang, Y. Shao, Y. Wu, S. Miao, *Adv. Energy Mater.* 10 (2020) 1902836.
- [6] G. Li, Z. Yang, Z. Yin, H. Guo, Z. Wang, G. Yan, Y. Liu, L. J. Li, *J. Mater. Chem. A* 7 (2019) 15541-15563.
- [7] J. Ding, W. Hu, E. Paek, D. Mitlin, *Chem. Rev.* 118 (2018) 6457-6498.
- [8] X. Yu, C. Zhan, R. Lv, Y. Bai, Y. Lin, Z. -H. Huang, W. Shen, X. Qiu, F. Kang, *Nano Energy* 15 (2015) 43-53.
- [9] M. Ashuri, Q. He, L. L. Shaw, *Nanoscale* 8 (2016) 74-103.
- [10] T. Zeng, X. Hu, P. Ji, Q. Peng, B. Shang, *Int. J. Electrochem. Sci.* 11 (2016) 10199-10209.

- [11] X. Li, Z. Yang, Y. Fu, L. Qiao, D. Li, H. Yue, D. He, *ACS Nano* 9 (2015) 1858-1867.
- [12] S. H. Lee, W. B. Kim, *J. Power Sources* 307 (2016) 38-44.
- [13] J. Liang, X. -Y. Yu, H. Zhou, H. B. Wu, S. Ding, X. W. D. Lou, *Angew. Chem. Int. Ed.* 53 (2014) 12803-12807.
- [14] W. Xie, Q. Wang, J. Xu, Y. Yu, R. Zhao, N. Li, M. Li, Y. Du, S. Peng, G. Cao, *J. Mater. Chem. A* 7 (2019) 10523-10533.
- [15] S. M. Jung, D. W. Kim, H. Y. Jung, *J. Mater. Chem. A* 8 (2020) 8244-8254.
- [16] J. Ma, J. Sung, Y. Lee, Y. Son, S. Chae, N. Kim, S. -H. Choi, J. Cho, *Adv. Energy Mater.* 10 (2020) 1903400.
- [17] Y. Yang, W. Yuan, W. Kang, Y. Ye, Y. Yuan, Z. Qiu, C. Wang, X. Zhang, Y. Ke, Y. Tang, *Nanoscale* 12 (2020) 7461-7484.
- [18] L. Yu, H. Hu, H. B. Wu, X. W. Lou, *Adv. Mater.* 29 (2017) 1604563.
- [19] Y. Sun, N. Liu, Y. Cui, *Nat. Energy* 1 (2016) 16071.
- [20] J. Sung, J. Ma, S. -H. Choi, J. Hong, N. Kim, S. Chae, Y. Son, S. Y. Kim, J. Cho, *Adv. Mater.* 31 (2019) 1900970.
- [21] X. Zhou, L. Yu, X. -Y. Yu, X. W. Lou, *Adv. Energy Mater.* 6 (2016) 1601177.
- [22] X. Zhou, L. Yu, X. W. Lou, *Adv. Energy Mater.* 6 (2016) 1600451.
- [23] B. Ludwig, Z. Zheng, W. Shou, Y. Wang, H. Pan, *Sci. Rep.* 6 (2016) 23150.
- [24] V. Wenzel, H. Nirschl, D. Nötzl, *Energy Technol.* 3 (2015) 692-698.
- [25] C. Cheng, R. Drummond, S. R. Duncan, P. S. Grant, *J. Power Sources* 448 (2020) 227376.
- [26] C. Cheng, R. Drummond, S. R. Duncan, P. S. Grant, *J. Power Sources* 413 (2019) 59-67.

- [27] S. H. Lee, C. Johnston, P. S. Grant, *Energy. Technol.* 8 (2020) 2000253.
- [28] J. Bu, P. Leung, C. Huang, S. H. Lee, P. S. Grant, *J. Mater. Chem. A* 7 (2019) 19094-19103.
- [29] S. H. Lee, C. Johnston, P. S. Grant, *ACS Appl. Mater. Interfaces* 11 (2019) 37859-37866.
- [30] S. H. Lee, K. Li, C. Huang, J. D. Evans, P. S. Grant, *ACS Appl. Mater. Interfaces* 11 (2019) 603-612.
- [31] S. H. Lee, A. Mahadevegowda, C. Huang, J. D. Evans, P. S. Grant, *J. Mater. Chem. A* 6 (2018) 13133-13141.
- [32] C. Huang, N. P. Young, J. Zhang, H. J. Snaith, P. S. Grant, *Nano Energy* 31 (2017) 377-385.
- [33] S. H. Lee, C. Huang, P. S. Grant, *Nano Energy* 61 (2019) 96-103.
- [34] L. Zhang, K. Zhang, Z. Shi, S. Zhang, *Langmuir* 33 (2017) 11164-11169.
- [35] Z. Qi, G. M. A Koenig Jr., *J. Power Sources* 33 (2016) 97-106.
- [36] S. H. Lee, E. J. Lim, Y. –R. Jo, B. –J. Kim, W. B. Kim, *ACS Appl. Mater. Interfaces* 6 (2014) 20634-20642.
- [37] S. H. Lee, G. Jo, W. Park, S. Lee, Y. –S. Kim, B. K. Cho, T. Lee, W. B. Kim, *ACS Nano* 4 (2010) 1829-1836.
- [38] G. Yang, S. –J. Park, *J. Mater. Chem. A* 8 (2020) 2627-2636.
- [39] H. S. Bhatti, D. H. Anjum, S. Ullah, B. Ahmed, A. Habib, A. Karim, S. K. Hasanain, *J. Phys. Chem. C* 120 (2016) 9553-9561.
- [40] Y. Yang, X. Zhao, H. –E. Wang, M. Li, C. Hao, M. Ji, S. Ren, G. Cao, *J. Mater. Chem. A* 6 (2018) 3479-3487.
- [41] J. G. Kim, S. H. Nam, S. H. Lee, S. M. Choi, W. B. Kim, *ACS Appl. Mater. Interfaces* 3 (2011) 828-835.

- [42] S. H. Lee, Y. -R. Jo, Y. Noh, B. -J. Kim, W. B. Kim, J. Power Sources 367 (2017) 1-7.
- [43] L. Yu, H. B. Wu, X. W. D. Lou, Adv. Mater. 25 (2013) 2296-2300.
- [44] S. H. Lee, C. Huang, C. Johnston, P. S. Grant, Electrochim. Acta 292 (2018) 546-557.
- [45] C. Han, Y. -B. He, M. Liu, B. Li, Q. -H. Yang, C. -P. Wong, F. Kang, J. Mater. Chem. A 5 (2017) 6368-6381.
- [46] S. H. Lee, C. Huang, P. S. Grant, Energy Storage Mater. 33 (2020) 408-415.
- [47] D. Y. W. Yu, C. Fietzek, W. Weydanz, K. Donoue, T. Inoue, H. Kurokawa, S. Fujitani, J. Electrochem. Soc. 154 (2007) A253-A257.
- [48] B. -R. Koo, K. -W. Sung, H. -J. Ahn, Adv. Funct. Mater. (2020) 2001863.
- [49] Y. Jiang, C. Hall, N. Song, D. Lau, P. A. Burr, R. Patterson, D. -W. Wang, Z. Ouyang, A. Lennon, ACS Appl. Mater. Interfaces 10 (2018) 42513-42523.
- [50] V. Augustyn, J. Come, M. A. Lowe, J. W. Kim, P. -L. Taberna, S. H. Tolbert, H. D. Abruña, P. Simon, B. Dunn, Nat. Mater. 12 (2013) 518.
- [51] B. -R. Koo, K. -W. Sung, H. -J. Ahn, Adv. Funct. Mater. 30 (2020) 2001863.
- [52] V. Augustyn, J. Come, M. A. Lowe, J. W. Kim, P. -L. Taberna, S. H. Tolbert, H. D. Abruña, P. Simon, B. Dunn, Nat. Mater. 12 (2013) 518.
- [53] Y. Sun, J. Tang, F. Qin, J. Yuan, K. Zhang, J. Li, D. -M. Zhu, L. -C. Qin, J. Mater. Chem. A 5 (2017) 13601-13609.
- [54] C. Huang, J. Zhang, H. J. Snaith, P. S. Grant, ACS Appl. Mater. Interfaces 8 (2016) 20756-20765.
- [55] Q. Zhao, Y. Zhang, Y. Meng, Y. Wang, J. Ou, Y. Guo, D. Xiao, Nano Energy 34 (2017) 408-420.

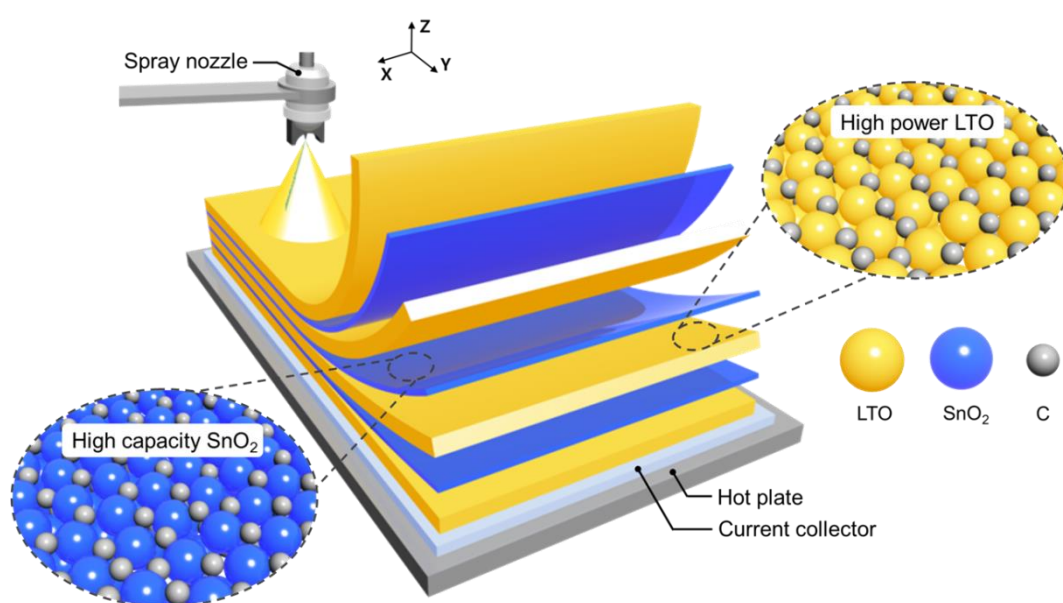


Figure 1. Graphical illustration of the layer-by-layer spray printing of high power LTO and high capacity SnO₂ into a multi-layered hetero-electrode. The left-hand and right-hand cartoons depict the idealized particle arrangement of SnO₂ and LTO within the multi-layer, respectively.

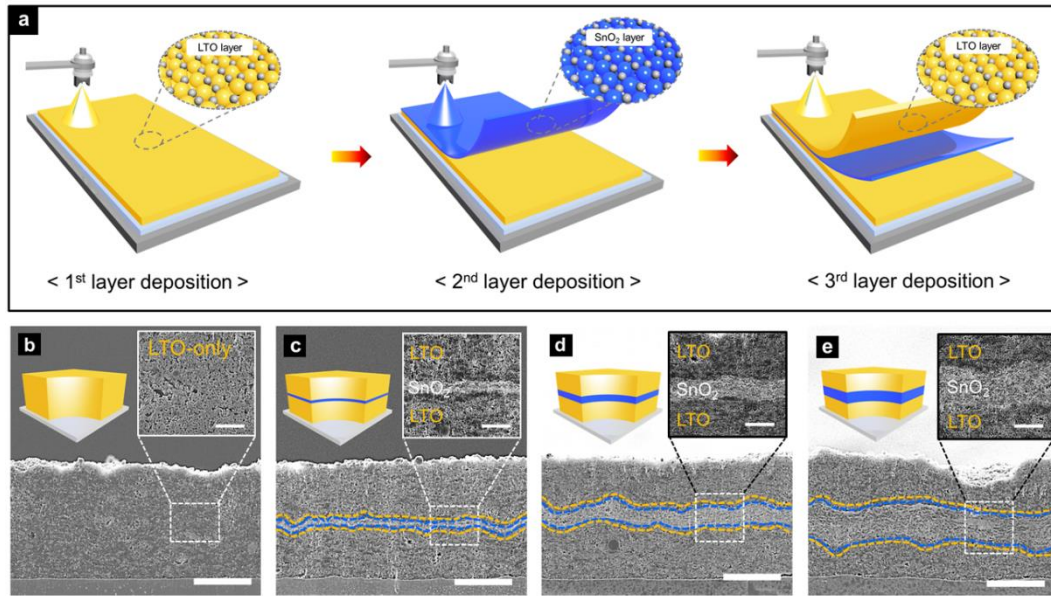


Figure 2. (a) A schematic procedure for the fabrication of a sandwich-type multi-layer structure by spray printing of discrete layers of LTO and SnO₂. Cross-section SEM images of the multi-layered electrodes with varying SnO₂ thickness: (b) 0 μm (LTO-only), (c) 2 μm, (d) 4 μm and (e) 6 μm. The scale bar indicates 10 μm. The left-hand cartoons show the intended variation in the SnO₂ thickness. The right-hand insets magnify a portion of the electrode cross-section. The inset scale bar indicates 5 μm.

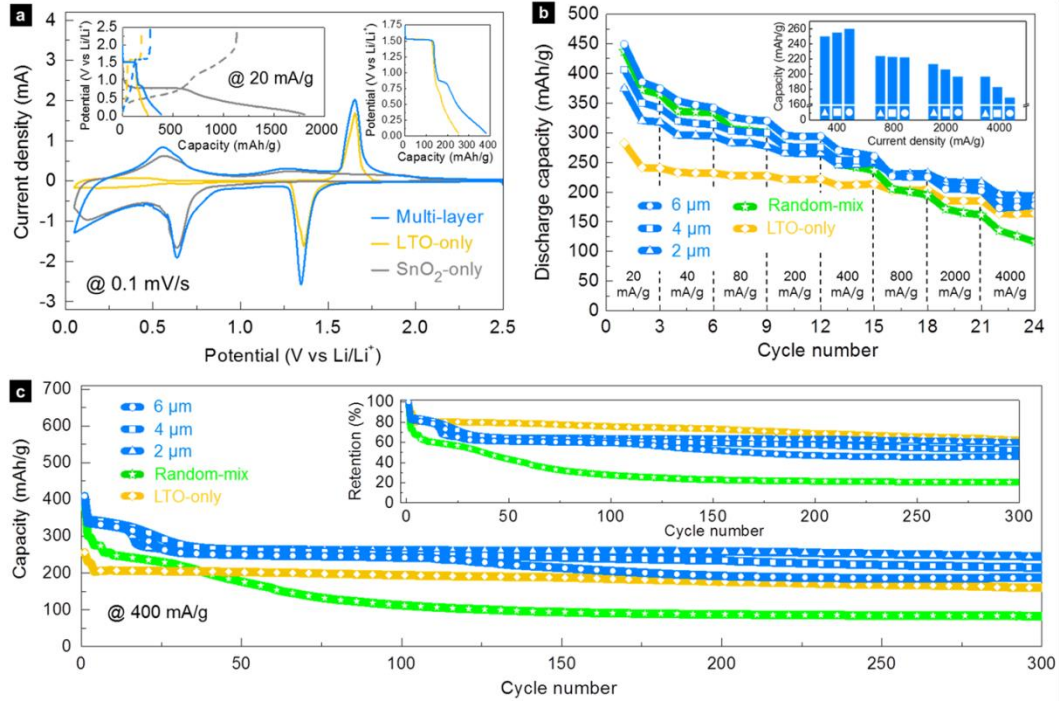


Figure 3. (a) Half-cell CV curves at a constant scan rate of 0.1 mV/s in the potential range 0.05 to 2.5 V (vs. Li/Li⁺) for LTO-only, SnO₂-only and the multi-layer electrode with a 6 μm SnO₂ layer. The insets show comparative charge/discharge curves at 20 mA/g for the same electrodes in the potential range 0.05 to 2.5 V (vs. Li/Li⁺). (b) Half-cell discharge capacity profiles at increasing current densities in the potential range 0.05 to 2.5 V (vs. Li/Li⁺). The inset bar graphs show the capacity degradation tendency as a function of the SnO₂ thickness. (c) Galvanostatic discharge capacity profiles at 400 mA/g in the voltage window 0.05 to 2.5 V (vs. Li/Li⁺) and the corresponding capacity retention (inset).

Table 1. Summary data for the spray printed LTO-based electrodes.

Electrode type	Mass loading (mg/cm ²)		Discharge capacity (mAh/g)			
	LTO	SnO ₂	20 mA/g	200 mA/g	2 A/g	4 A/g
LTO-only	3.12 ± 0.04	-	241	221	185	163
LTO + 2 µm SnO ₂	2.98 ± 0.04	0.18 ± 0.02	321	266	217	196
LTO + 4 µm SnO ₂	2.81 ± 0.02	0.37 ± 0.01	350	277	211	185
LTO + 6 µm SnO ₂	2.67 ± 0.02	0.58 ± 0.02	386	295	206	178
LbL	2.65 ± 0.03	0.57 ± 0.02	381	300	234	206
Random-mix	3.21 ± 0.05 (80 % LTO + 20 % SnO ₂)		382	277	172	135

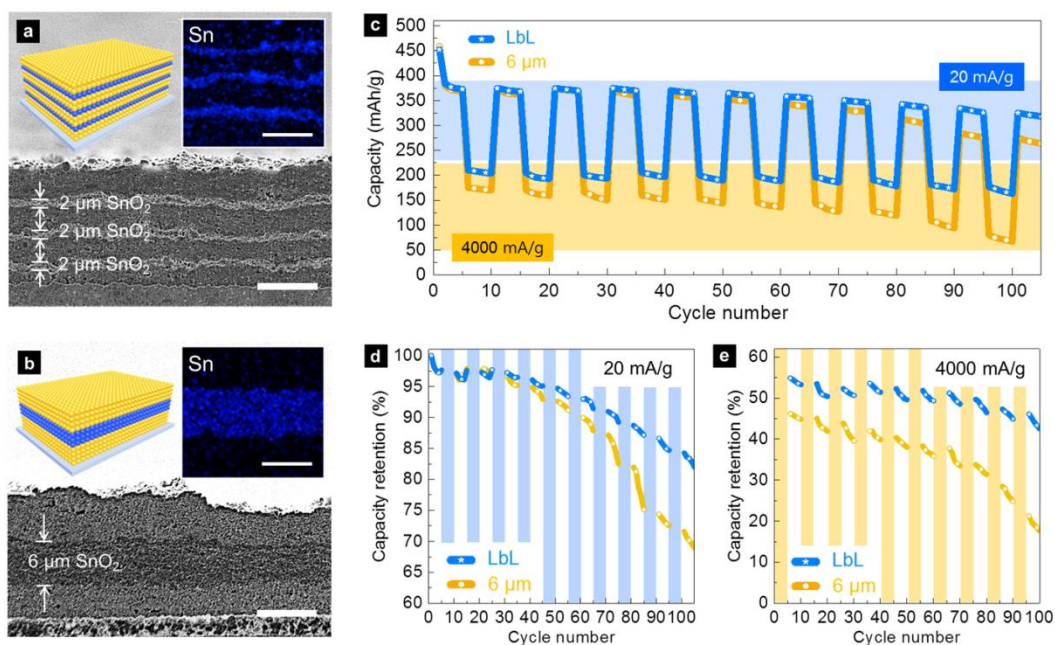


Figure 4. Cross-section SEM images of (a) the LbL electrode and (b) the multi-layer electrode with a single 6 μm SnO₂ layer. The scale bar indicates 10 μm. The left-upper cartoons show the different SnO₂ arrangements, and the right-hand insets show the EDS elemental maps for Sn in the multi-layers. The inset scale bar indicates 5 μm. (c) Gravimetric half-cell discharge capacity profiles at 20 mA/g and 4000 mA/g in the potential range 0.05 to 2.5 V (vs. Li/Li⁺). Corresponding capacity retention profiles for (d) 20 mA/g and (e) 4000 mA/g.

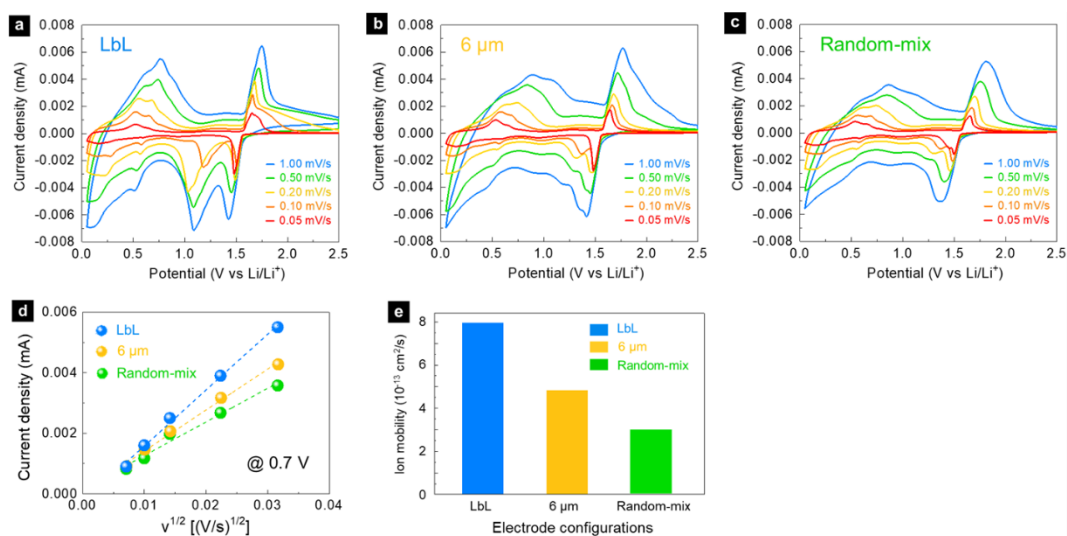


Figure 5. (a-c) CV profiles for the LbL, 6 μm SnO_2 multi-layer and random-mix electrodes at various scan rates of 0.05 to 1.0 mV/s in the potential range 0.0 to 2.5 V (vs. Li/Li^+). (d) The linear relationship between the anodic peak current density at approximately 0.7 V and the square root of the scan rate for the same electrodes. (e) Corresponding effective lithium ion mobility for SnO_2 .

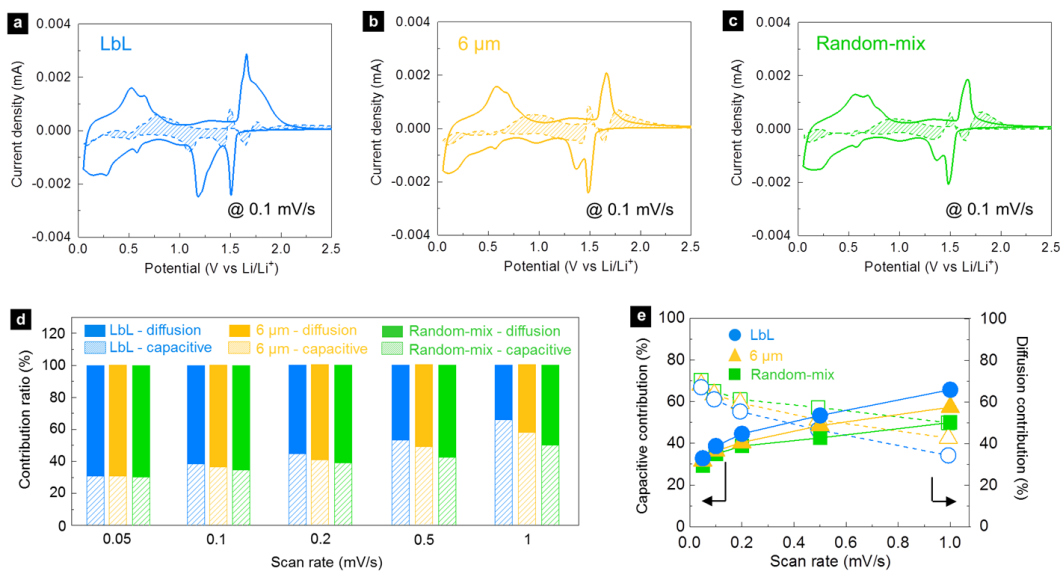


Figure 6. Capacitive-controlled electrode responses (the patterned areas) at 0.1 mV/s for (a) the LbL, (b) the multi-layer with a single 6 μm SnO₂ layer and (c) the random-mix electrode. (d) Comparative bar graphs show the ratio of the capacitive-to-diffusion contribution for the same electrodes as a function of CV scan rates. (e) The scan rate-dependent variation in the ratio of capacitive- and diffusion-controlled contributions.

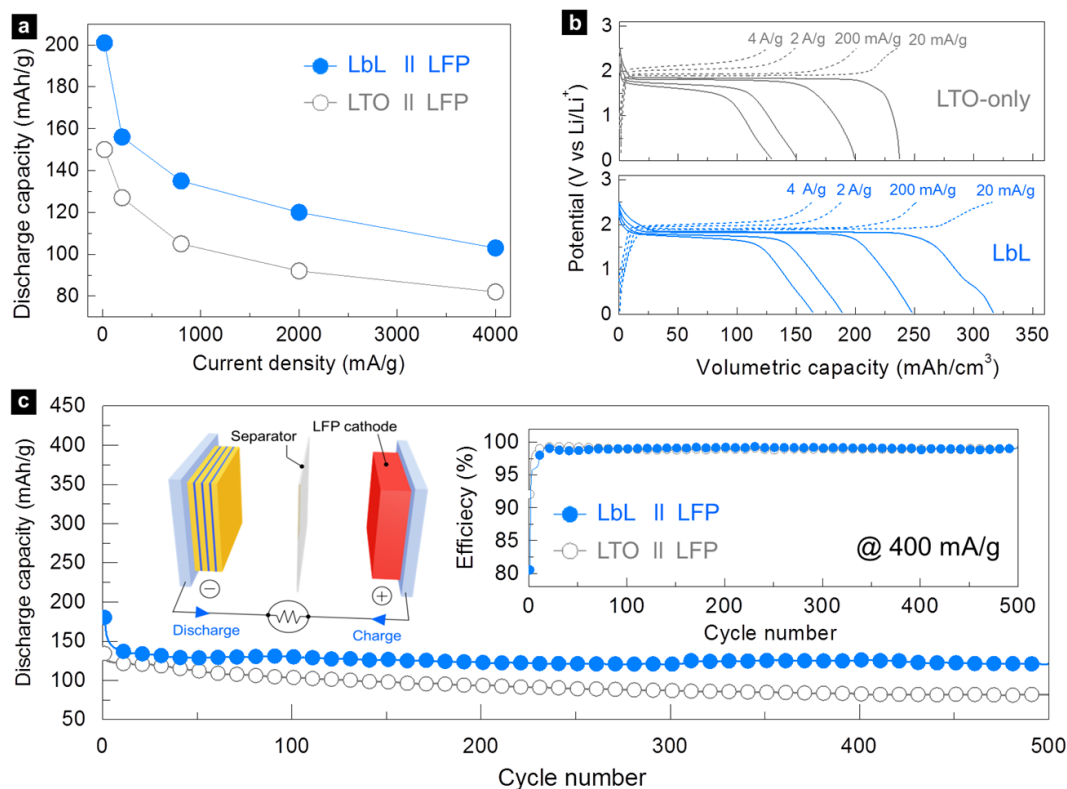


Figure 7. (a) Gravimetric discharge capacity profiles for LIB cells using the LbL and LTO-only electrodes in the potential range 0.05 to 2.5 V (vs. Li/Li⁺). (b) Comparative volumetric charge/discharge profiles for the same LIB cells in the voltage window 0.05 to 2.5 V (vs. Li/Li⁺). (c) LIB Galvanostatic discharge capacity profiles at 400 mA/g in the voltage window 0.05 to 2.5 V (vs. Li/Li⁺) and the corresponding coulombic efficiency plots (the right-hand inset). The left-hand cartoon depicts the LIB arrangement using a LbL negative electrode.

Table 2. Summary data for the LIB cells using the LbL and LTO-only electrodes.

Anode type	Mass loading (mg/cm ²)		Discharge capacity (mAh/g)			
	Anode (SnO ₂)	Cathode	20 mA/g	200 mA/g	2 A/g	4 A/g
LTO-only	3.12 ± 0.04 (0.00)	3.14 ± 0.02	150	127	92	82
LbL	3.13 ± 0.03 (0.45)	4.67 ± 0.04	201	157	120	103

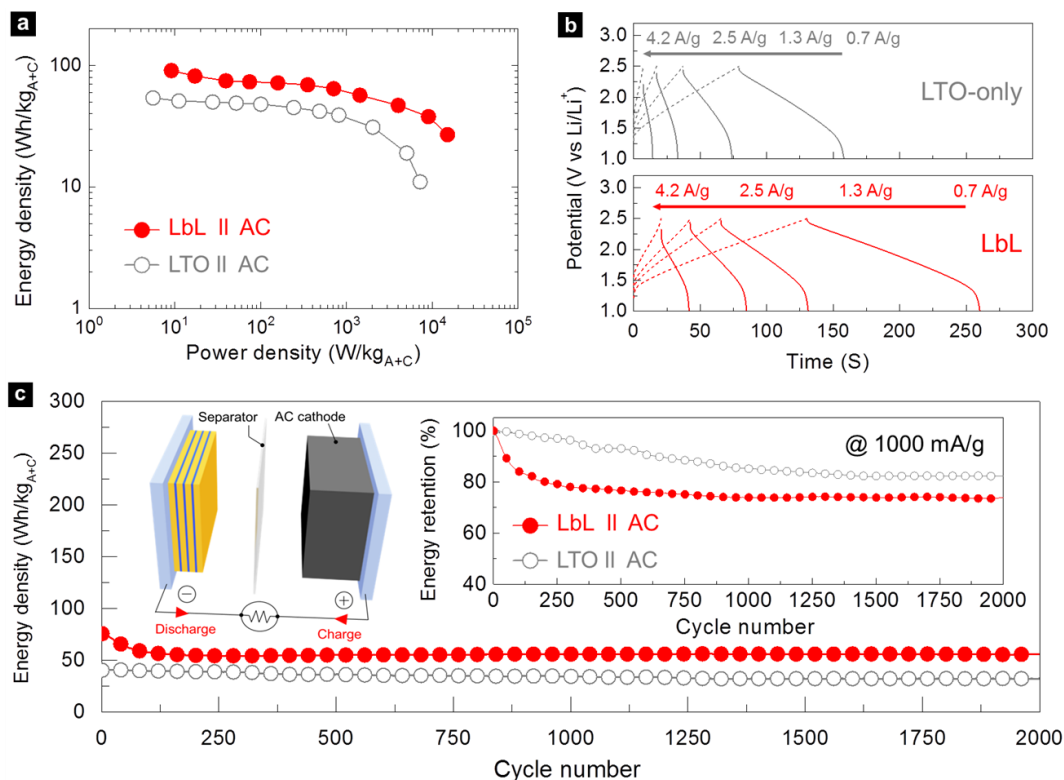


Figure 8. (a) Comparative Ragone plots for LIC cells using the LbL and LTO-only electrodes. (b) Comparative charge/discharge curves of the same LIC cells at various current densities in the voltage window 1.0 to 2.5 V (vs. Li/Li⁺). (c) Galvanostatic LIC discharge energy density profiles at 1000 mA/g in the voltage window 1.0 to 2.5 V (vs. Li/Li⁺) and the corresponding energy density retention (the right-hand inset). The left-hand cartoon shows the LIC comprising a LbL negative electrode and a spray printed AC-based positive electrode.

Table 3. Summary data for LIC cells using the LbL and LTO-only electrodes.

Anode type	Mass loading (mg/cm ²)		Capacitance (F/g)			
	Anode (SnO ₂)	Cathode	0.7 A/g	1.3 A/g	2.5 A/g	4.2 A/g
LTO-only	3.12 ± 0.04 (0.00)	12.52 ± 0.02	37	32	27	17
LbL	3.13 ± 0.03 (0.45)	12.53 ± 0.03	62	55	48	35

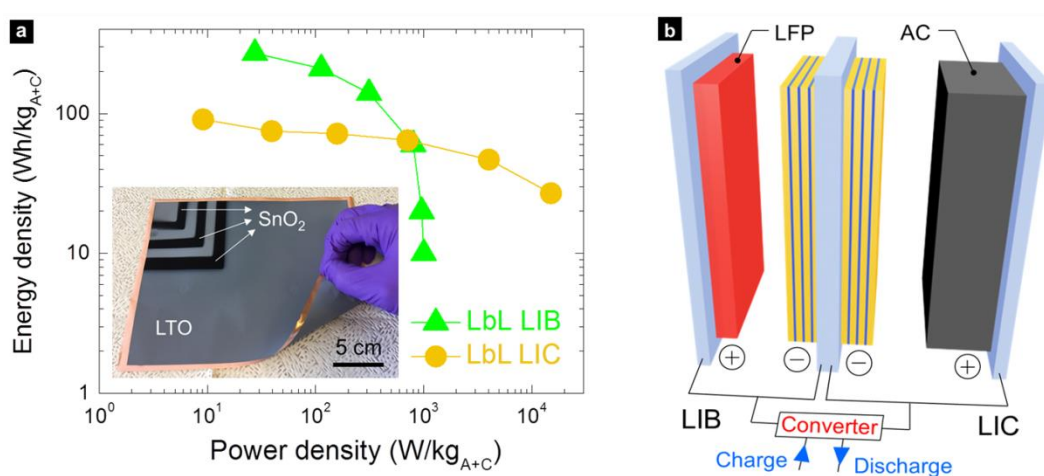


Figure 9. (a) Comparative Ragone plots for the LIB and LIC cells, both using a LbL negative electrode. The inset photograph shows a double-sided fabrication of the LbL electrode over a 20 × 20 cm² Cu current collector in a patterned configuration. (b) The schematic diagram depicts a model device where the LIB and LIC configuration are combined by a large-area, double-sided LbL negative electrode.

Supporting Information

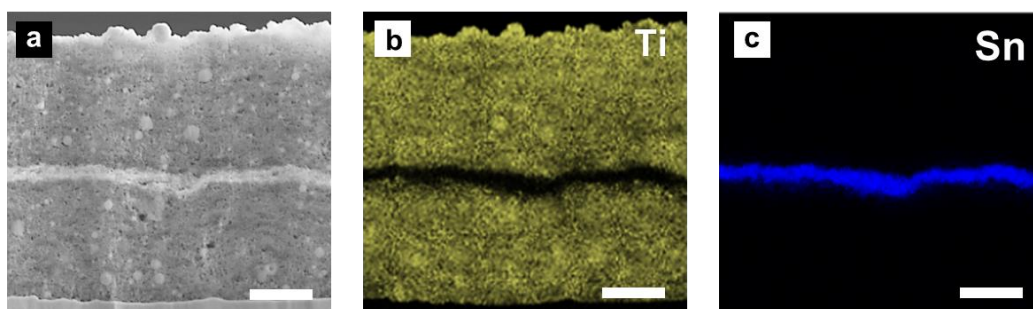


Figure S1. (a) Cross-section SEM image of a LTO-based multi-layer electrode with a 2 μm SnO_2 inter-layer. The corresponding EDS maps for (b) Ti (yellow) and (c) Sn (blue) within the multi-layer. The scale bar indicates 5 μm .

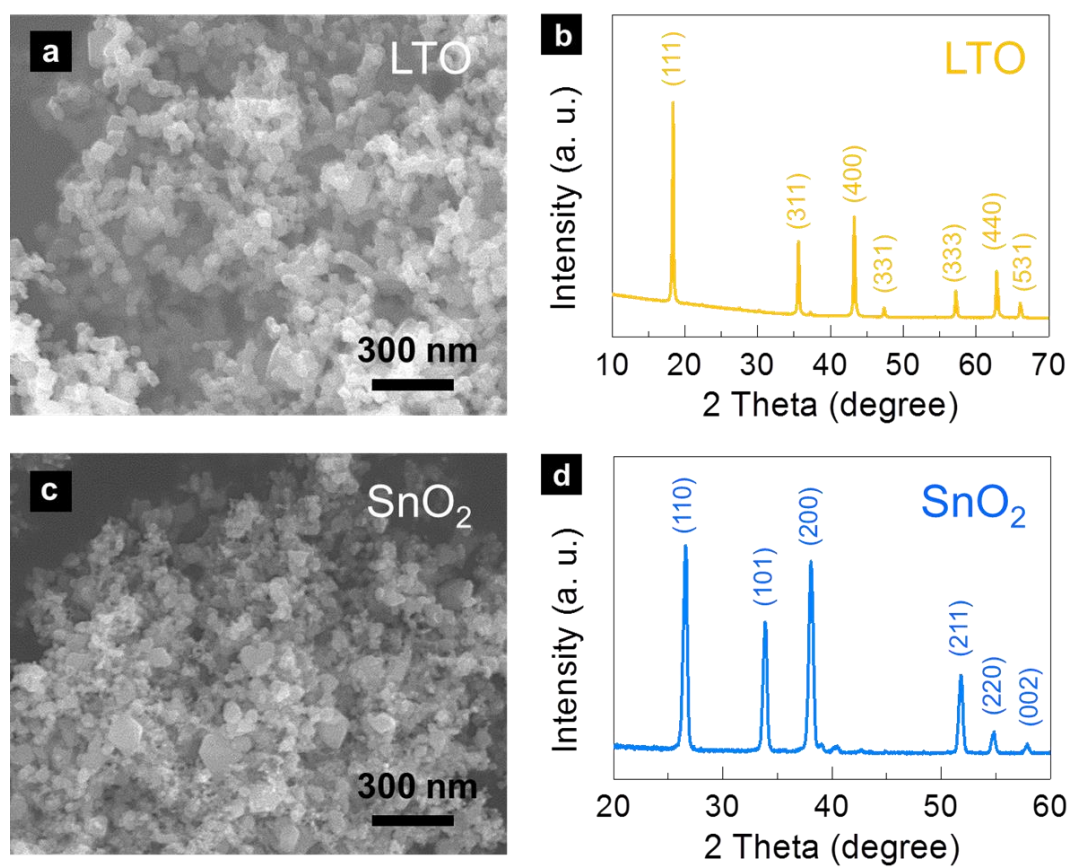


Figure S2. (a) SEM image of ~ 80 nm diameter pristine LTO particles. (b) Corresponding XRD pattern typical of spinel LTO. (c) SEM image of ~ 50 nm pristine SnO₂ particles. (d) Corresponding XRD patterns typical of rutile SnO₂.

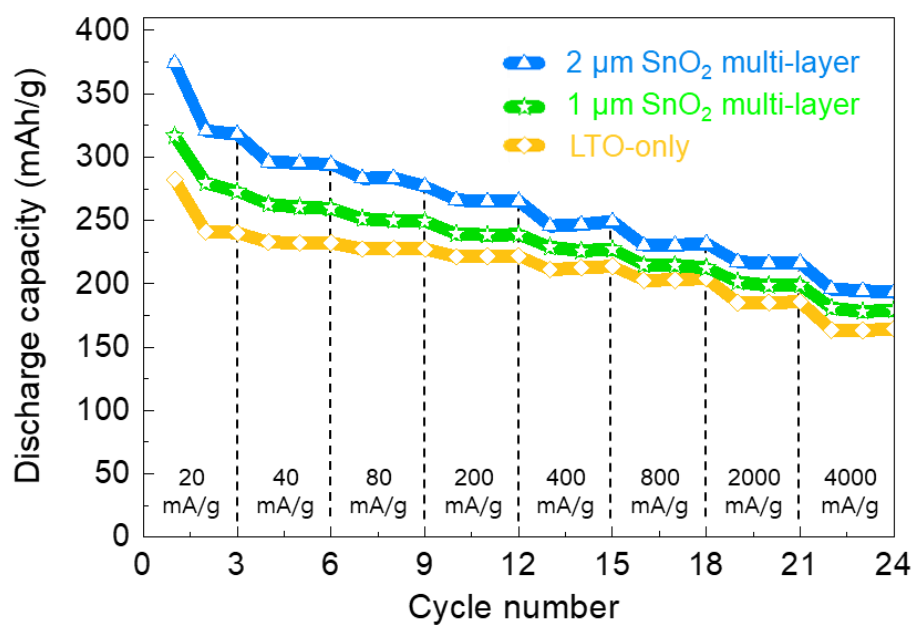


Figure S3. Comparative half-cell discharge capacity profiles at increasing current densities in the potential range 0.05 to 2.5 V (vs. Li/Li⁺) for the LTO-only and the multi-layer electrodes with 1 μm and 2 μm SnO₂.

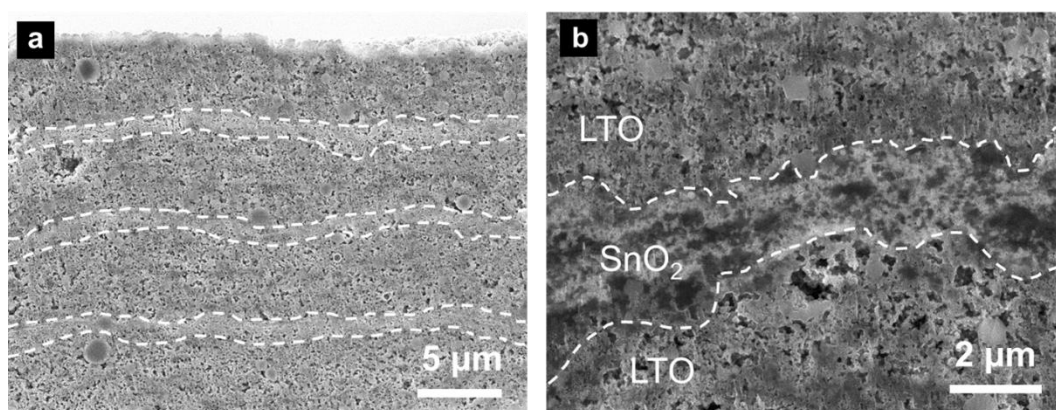


Figure S4. (a) Cross-section SEM image for the LbL electrode after repeated 105 charge/discharge cycles. (b) The magnified image for a portion of the SnO_2 layer.

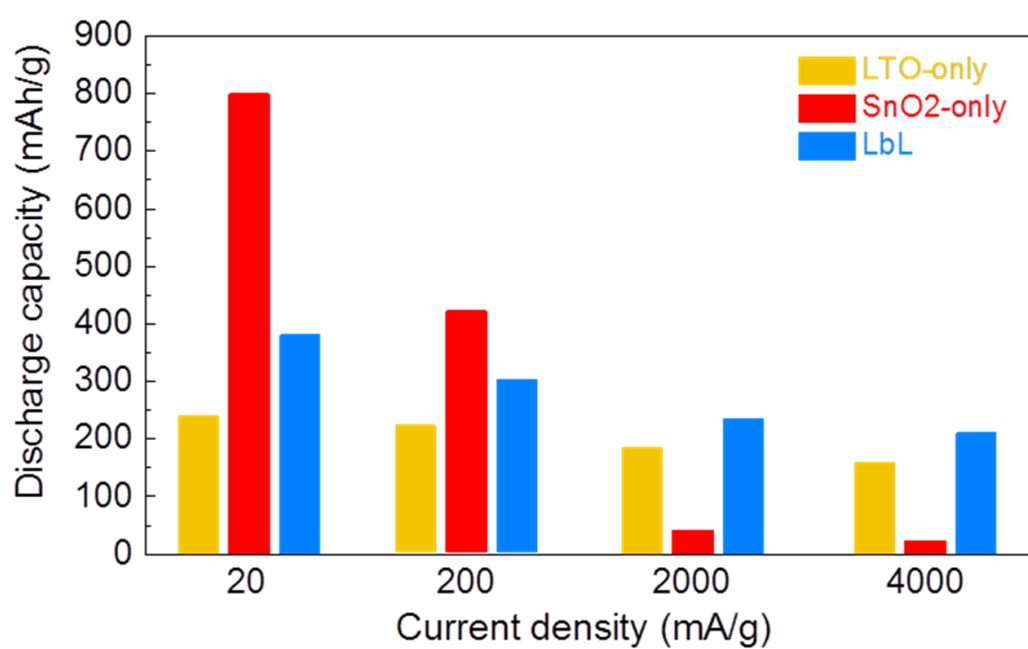


Figure S5. Comparative discharge capacity at various current densities in the potential range 0.05 to 2.5 V (vs. Li/Li⁺) for LTO-only, SnO₂-only and LbL electrodes.

Table S1. Summary data for LTO-only, SnO₂-only and LbL electrodes.

Electrode type	Mass loading (mg/cm ²)		Thickness (μm)
	LTO	SnO ₂	
LTO-only	3.12 ± 0.04	-	40 ± 4
SnO ₂ -only	-	0.60 ± 0.04	6 ± 1
LbL	2.65 ± 0.03	0.57 ± 0.02	41 ± 5

Table S2. Comparative performance of multi-component LTO-based electrodes.

Materials combination	Rate performance	Reference
LbL	~ 210 mAh/g @ 4 A/g	This work
LTO/Si composite	~ 100 mAh/g @ 7 A/g	R1
LTO/Si composite	~ 50 mAh/g @ 4 C	R2
LTO/Sn composite	~ 170 mAh/g @ 0.5 A/g	R3
LTO/Sn composite	~ 180 mAh/g @ 2.5 A/g	R4
LTO/SnO ₂ composite	~ 270 mAh/g @ 5 C	R5
LTO/SnO ₂ composite	~ 440 mAh/g @ 1.7 A/g	R6

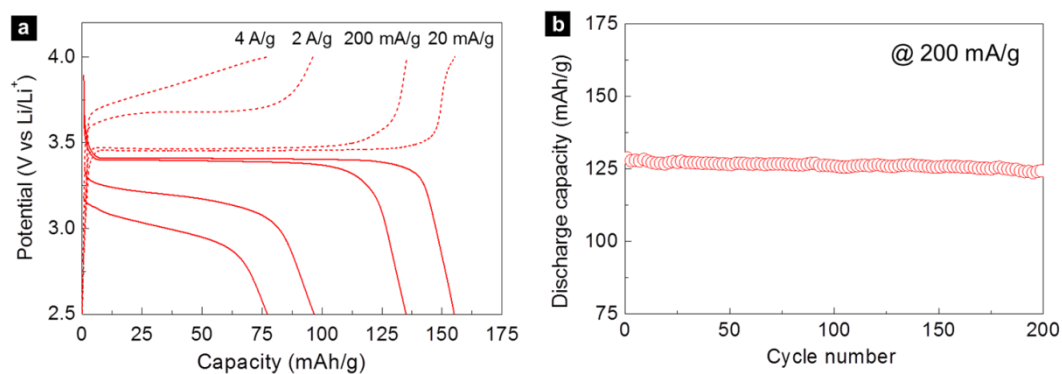


Figure S6. (a) Gravimetric half-cell charge/discharge curves of spray printed LFP electrodes at various charge/discharge current densities of 20 to 4000 mA/g in the potential range 2.5 to 4.0 V (vs. Li/Li⁺). (b) Galvanostatic discharge capacity profile of the same LFP electrode at a constant current density of 200 mA/g in the potential range 2.5 to 4.0 V (vs. Li/Li⁺).

Table S3. Summary data for a spray printed LFP electrode.

Formulation (LFP : SP : CMC)	Mass loading (mg/cm ²)	Thickness (μm)	Discharge capacity (mAh/g)			
			20 mA/g	200 mA/g	2 A/g	4 A/g
80 : 10 : 10	3.53 ± 0.03	50 ± 2	155	135	95	78

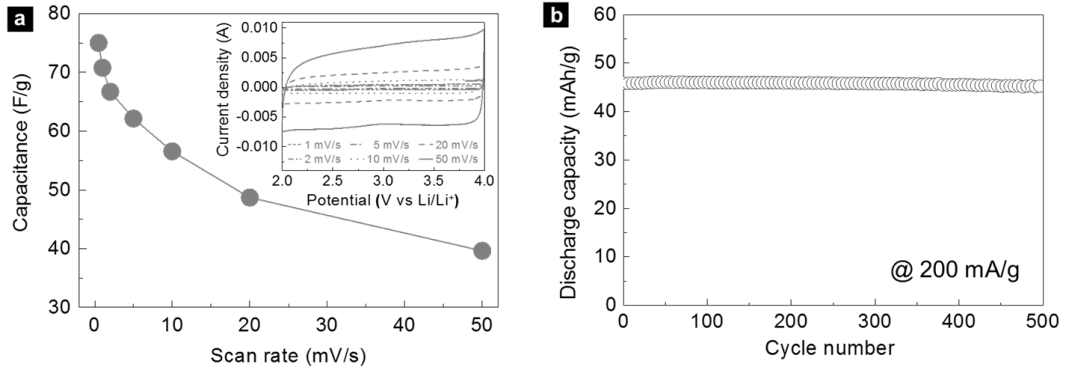


Figure S7. (a) Specific half-cell capacitance profile for the spray printed AC-based electrode, which was estimated from the CV curves (the inset) according to:

$$C = \frac{1}{mv(V_a - V_c)} \int_{V_a}^{V_c} I(V) dV$$

where C was the specific capacitance [F/g], m was the total electrode mass [g], v was the scan rate [V/s], $V_a - V_c$ was the potential window [V], and I was the charging current [A]. The inset shows CV profiles at increasing scan rates of 1 to 50 mV/s in the potential range 2.0 to 4.0 V (*vs.* Li/Li⁺). (b) Galvanostatic discharge capacity profile of the AC-based electrode at a constant current density of 200 mA/g in the potential range 2.0 to 4.0 V (*vs.* Li/Li⁺).

Table S4. Summary data for the spray printed AC-based electrode.

Formulation (AC : SP : CMC)	Mass loading (mg/cm ²)	Capacitance (F/g)			
		0.5 mV/s	5 mV/s	20 mV/s	50 mV/s
80 : 10 : 10	12.53 ± 0.03	76	62	50	40

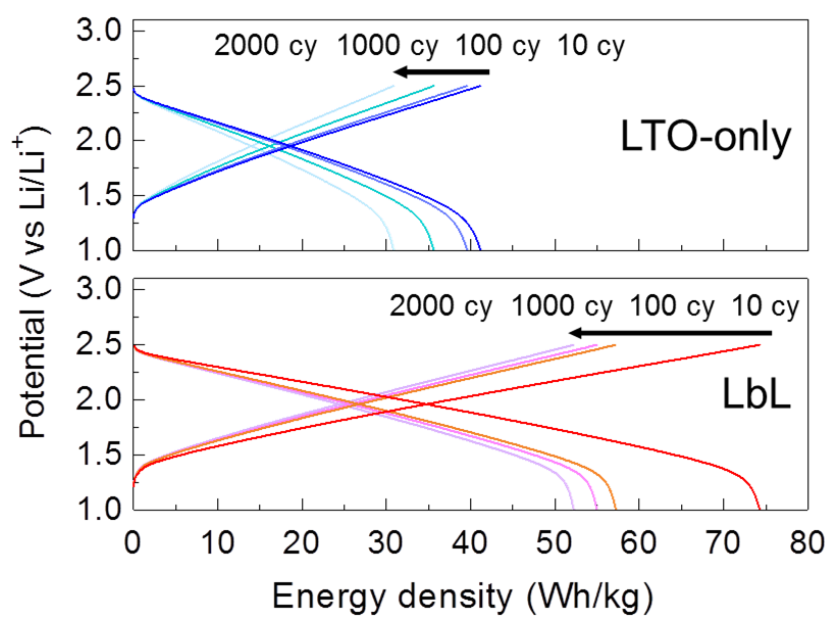


Figure S8. Comparative charge/discharge energy density curves at a constant current density of 1000 mA/g in the voltage window 1.0 to 2.5 V (vs. Li/Li^+) for LICs using the LTO-only and LbL negative electrodes.

References

- R1. C. Chen, R. Agrawal, C. Wang, *Nanomaterials* 5 (2015) 1469-1480.
- R2. Y. Lin, Y. Yang, Y. Lin, G. Zhao, T. Zhou, Z. Huang, *Int. J. Electrochem. Sci.* 6 (2011) 5588-5596.
- R3. T. Zeng, X. Hu, P. Ji, Q. Peng, B. Shang, *Int. J. Electrochem. Sci.* 11 (2016) 10199-10209.
- R4. R. Cai, X. Yu, X. Liu, Z. Shao, *J. Power Sources* 195 (2010) 8244-8250.
- R5. A. K. Haridas, C. S. Sharma, N. Y. Hebalkar, T. N. Rao, *Materials Today Energy* 4 (2017) 14-24.
- R6. K. M. Yang, Y. J. Hong, S. H. Choi, B. K. Park, Y. C. Kang, *Int. J. Electrochem. Sci.* 8 (2013) 1026-1040.